arXiv:2305.03621v1 [astro-ph.SR] 5 May 2023

Influence of the Lower Atmosphere on Wave Heating and Evaporation in Solar Coronal Loops

Mingzhe Guo,[1] Timothy Duckenfield,[2] Tom Van Doorsselaere,[1]
Konstantinos Karampelas,[1] Gabriel Pelouze,[3] and Yuhang Gao[4,1]

[1]Centre for mathematical Plasma Astrophysics, Department of Mathematics, KU Leuven, Celestijnenlaan 200B,
B-3001 Leuven, Belgium

[2]Department of Mathematics, Physics and Electrical Engineering, Northumbria University, Newcastle upon Tyne,
NE1 8ST, UK

[3]Université Paris-Saclay, CNRS, Institut d'astrophysique spatiale, 91405, Orsay, France

[4]School of Earth and Space Sciences, Peking University, Beijing, 100871, China

ABSTRACT

We model a coronal loop as a three-dimensional magnetic cylinder in a realistic solar atmosphere that extends from the chromosphere to the corona. Kink oscillations, believed ubiquitous in the solar corona, are launched in the loop. Heating is expected due to the dissipation of wave energy at small structures that develop from the Kelvin-Helmholtz instability induced by kink oscillations. Increases in temperature and internal energy can be observed in the coronal counterpart of the driven loop. With the presence of thermal conduction, chromospheric evaporation can also be seen. Although the volume averaged temperature and density changes seem slight ($\sim 4\%$ relative to a non-driven loop), the enthalpy flow from the lower atmosphere redistributes the density

Corresponding author: Mingzhe Guo, Timothy Duckenfield
mingzhe.guo@kuleuven.be, tim.duckenfield@northumbria.ac.uk

and temperature in the vertical direction, thus enhancing the dissipation of wave energy in the corona. The efficient heating in the coronal counterpart of the loop can complement the thermal conductive losses shown in the current model and thus maintain the internal energy in the corona.

1. INTRODUCTION

More and more observations have confirmed the omnipresence of kink waves in coronal loops (e.g., Nakariakov & Kolotkov 2020; Nakariakov et al. 2021, for recent reviews) and thus bring kink waves into the forefront of coronal heating consideration (see De Moortel & Nakariakov 2012; Arregui 2015; Van Doorsselaere et al. 2020, for recent reviews). In the heating process, effective dissipation of wave energy can be achieved when the Lundquist number and Reynolds number, which are typically very large ($\sim 10^{12}$) in the solar corona, become very small (Soler & Terradas 2015). Thus efficient heating relies on the occurrence of small spatial scales. Generally, kink waves are believed to suffer resonant absorption (see Goossens et al. 2011, for a review) that transfers wave energy from collective kink modes to local Alfvén waves with the occurrence of transverse inhomogeneity around the loop boundary (e.g., Guo et al. 2020). The converted localized azimuthal Alfvén waves undergo phase mixing (e.g., Heyvaerts & Priest 1983). The subsequent phase mixed Alfvén waves can enhance the Kelvin-Helmholtz instability (KHI, Browning & Priest 1984), which is induced by velocity shear between loops and the background corona, thereby facilitating the wave dissipation by further generating smaller scales. This scenario is first demonstrated by Ofman et al. (1994) in coronal loop models. Recently, numerical progress confirmed that transverse waves in coronal loops can induce the KHI, forming the TWIKH rolls (Transverse Wave Induced Kelvin-Helmholtz rolls, see e.g., Terradas et al. 2008; Antolin et al. 2015; Karampelas et al. 2017; Howson et al. 2017; Guo et al. 2019a,b; Shi et al. 2021). Non-linear damping of kink waves associated with the KHI has been investigated numerically by e.g., Magyar & Van Doorsselaere (2016) and analytically by e.g., Van Doorsselaere et al. (2021). During such a process, the energy of collective kink waves can dissipate at such turbulent small structures, and quantitative evaluations of heating effects have been made

by e.g., Karampelas et al. (2017, 2019); Guo et al. (2019a,b). Recent numerical progress shows that the heating effects induced by kink waves can balance the radiative loss in the solar corona (Shi et al. 2021; De Moortel & Howson 2022), which shed new light on understanding coronal heating from the perspective of waves.

The influence of chromospheric evaporation on the heating of coronal loops was first considered by Ofman et al. (1998) based on resonant kink waves. However, the aforementioned investigations associated with TWIKH rolls mainly focus on the coronal counterpart of loops. In reality, the lower atmosphere can act as a mass and energy reservoir for physical processes in the corona. In the process associated with impulsive heating, nanoflares (Parker 1988) for instance, enthalpy flux plays an important role in the thermal evolution of coronal loops (e.g., Bradshaw & Cargill 2010; Cargill et al. 2012). Regarding the AC models, Ohmic heating has been confirmed by both observations (Van Doorsselaere et al. 2007) and numerical simulations (Karampelas et al. 2019; Guo et al. 2019b) in coronal loops. In such a scenario, wave heating is expected to happen near loop footpoints, where the current density that is essential for resistive dissipation has maximum values at loop ends (Van Doorsselaere et al. 2007). In this way, the cooler chromosphere can be heated straightforwardly. Given this, a natural question arises: Can the heating near loop footpoints trigger chromosphere evaporation? The scenario of evaporation is usually discussed when chromospheric materials are heated during such energy release processes as solar flares (e.g., Fisher et al. 1985; Milligan et al. 2006; Tian & Chen 2018). Although the energy dissipation of waves is not so fierce as flares, gentle chromosphere evaporations are still expected (Fisher et al. 1985). The influence of such evaporation flows on the efficiency of wave heating in the corona remains to be evaluated in recent models. Recent progress by Van Damme et al. (2020) investigated the influence of chromosphere evaporation on the phase mixing of Alfvén waves in a two-dimensional coronal loop model. The density shell around the loop boundary that is essential for energy dissipation of Aflvén waves seems not significantly changed in the modest heating process. However, wave energy dissipation happens over almost the whole deformed cross-section of loops when it comes to transverse oscillations (e.g., Karampelas &

Van Doorsselaere 2018; Guo et al. 2019a,b). It remains to be seen how chromosphere evaporation influences wave energy dissipation in coronal loops deformed by kink oscillations.

In this paper, we aim to investigate the influence of the lower atmosphere on coronal heating effects. The paper is organized as follows. Section 2 describes the model, including the equilibrium and numerical setup. In Section 3, we present the numerical results. Section 4 summarizes our findings, ending with some further discussion.

2. NUMERICAL MODEL

We use a similar magnetic flux tube employed in Pelouze et al. (2023, P23), with the key difference that we simulate half of a closed loop with both footpoints anchored in the chromosphere. The model is initiated from a 2D hydrostatic equilibrium in cylindrical coordinates (r, z). A loop-oriented gravity $g(z) = -g_\odot \sin\left[\pi(L - z)/(2L)\right]$ is considered, with $L = 100$Mm being the half length of the loop. The initial magnetic field is $\boldsymbol{B} = B_0\hat{z}$, with B_0 set to 42G. The temperature profile, derived from Aschwanden & Schrijver (2002), is given by

$$T(r, z) = \begin{cases} T_{\text{ch}}, & z \leq z_{\text{ch}}, \\ T_{\text{ch}} + [T_{\text{co}}(r) - T_{\text{ch}}] \left[1 - \left(\dfrac{L - z}{L - z_{\text{ch}}}\right)^2\right]^{0.3}, & z > z_{\text{ch}}, \end{cases} \tag{1}$$

where $T_{\text{ch}} = 20000$K is the temperature of the chromosphere, and $z_{\text{ch}} = 4$Mm represents its thickness. The transverse temperature profile is defined as

$$T_{\text{co}}(r) = T_{\text{e}} + \frac{1}{2}(T_{\text{i}} - T_{\text{e}})\left\{1 - \tanh\left[\left(\frac{r}{R} - 1\right)b\right]\right\}, \tag{2}$$

where $T_{\text{i}} = 1.2$MK ($T_{\text{e}} = 3.6$MK) is the temperature inside (outside) the tube. $R = 1$Mm gives the radius of the loop, and $b = 10$ defines the thickness of the inhomogeneous layer, corresponding to $l/R = 0.6$ at the loop bottom. The transverse distribution of the density in Figure 1a clearly shows the variation of this layer thickness along the height. The initial state is not in magnetohydrostatic balance, thus a relaxation is needed. In this stage, we redefine the velocity rewrite layer, which was proposed in P23 to absorb the upward flows in the loop. With the presence of the velocity rewrite layer, the large flow induced by the initial state, which is not in magnetohydrostatic balance, is

weakened. Thus the process of reaching an equilibrium becomes more gradual and gentle, ensuring the stability of the simulation. The velocity is modified as $v'(r, z) = \alpha(t)v_i(r, z)$. The parameter $\alpha(t)$ is defined as

$$
\alpha(t) = \begin{cases} 0.9995 + 0.0005\dfrac{t}{t_c}, 0 < t \le t_{\rm c}, \\ 1, \qquad\qquad\quad t > t_{\rm c}, \end{cases} \tag{3}
$$

where $t_{\rm c} = 37.3\text{ks}$ represents the critical time. The vertical velocity in the loop is then suppressed to be less than 1.3kms^{-1} and significant quantity changes (e.g., a drop in magnetic field strength in P23 [1]) are avoided after the relaxation. The relaxed state is then straightforwardly converted to 3D by rotating the 2D axisymmetric results. To avoid any unphysical oscillations due to boundary changes from the 2D cylindrical coordinate to the 3D Cartesian domain, we allow the 3D system to relax for another 2.8ks. The initial temperature and density distributions of the loop axis of the 2D and 3D simulations are shown in Figure 2.

Note that this simulation is gravitationally stratified, leading to the transverse structuring of the loop changing with height. As shown in Figure 1b, the inhomogeneous layer thickness is smaller at the loop apex ($z = 100\text{Mm}$) than at lower heights. One may expect this change in layer thickness to have an impact on the formation of KHI (e.g., Magyar & Van Doorsselaere 2016).

The chromosphere and transition region are included in the current model. The transition region has been artificially broadened to ensure its resolution, following the scheme developed by Linker et al. (2001); Lionello et al. (2009); Mikić et al. (2013). As described in P23, a critical temperature $T_{\rm c} = 2.5 \times 10^5\text{K}$ is defined, below (above) which the parallel thermal conductivity is $\kappa_\parallel = \kappa_0 T_{\rm c}^{5/2}$ ($\kappa_\parallel = \kappa_0 T^{5/2}$), with κ_0 being $5.6 \times 10^{-7}\text{erg cm}^{-1}\text{ s}^{-1}\text{ K}^{-7/2}$. This modified thermal conductivity changes the temperature length scale in the vertical direction, thus leading to a significant broadening of the transition region after relaxation, see also Van Damme et al. (2020) and P23. Therefore, a coarser resolution in the vertical direction is allowed in the current simulation.

---

[1] In the current model, the magnetic field undergoes a slight change from the initial value of 42G to around 40G after relaxation.
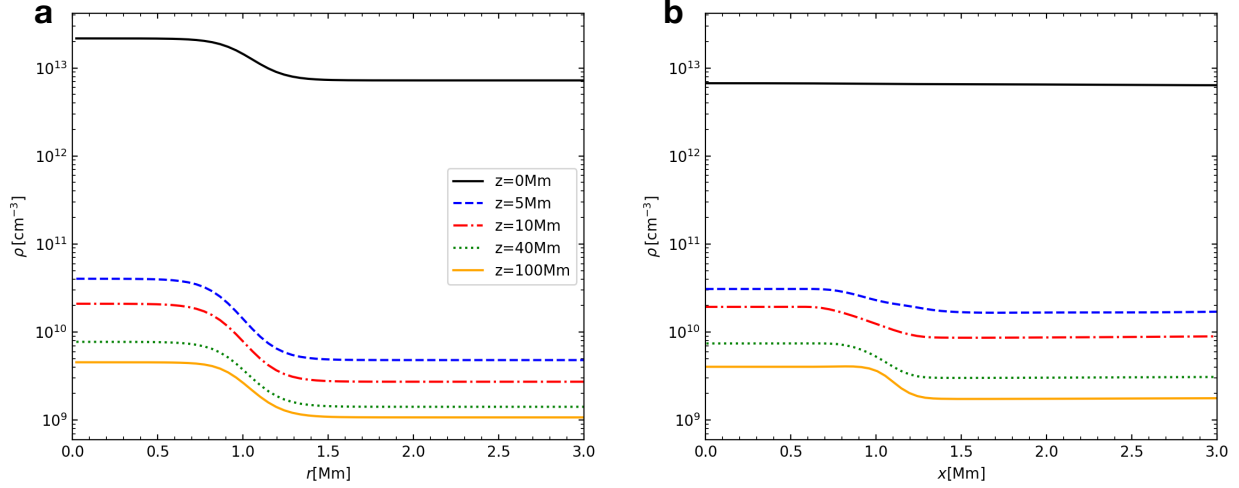
Figure 1. Transverse distribution of the density along the r-direction in the 2D simulation (left) and x-direction in the 3D simulation (right). The left panel represents the initial density in the 2D simulation. The right panel shows the initial state of the 3D simulation after relaxation. Different colors represent different heights.
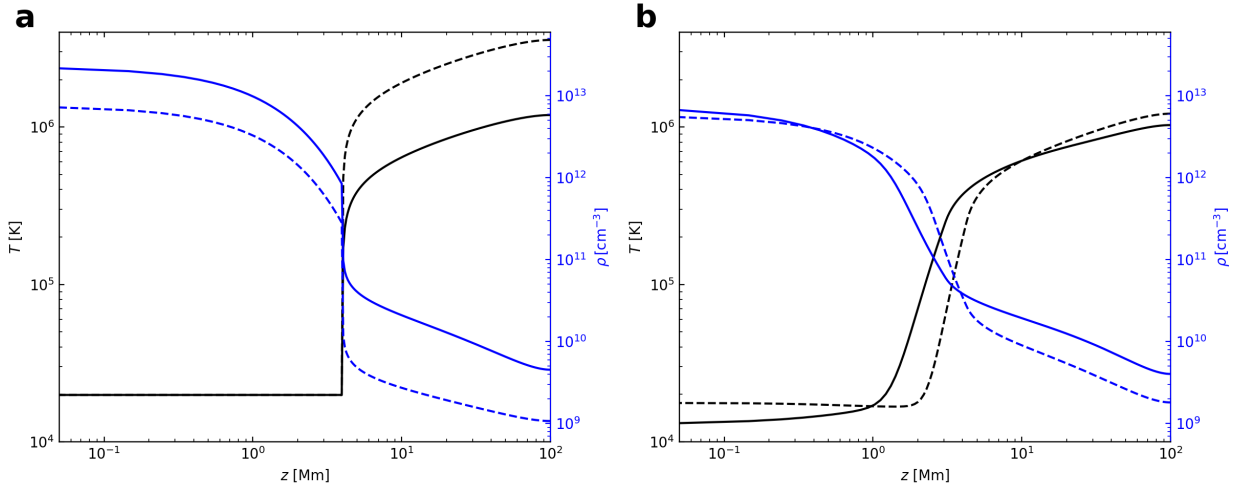

Figure 2. Spatial distribution of temperature and density along the z-direction. The left panel displays the initial quantities before relaxation in the 2D equilibrium. The right panel shows the initial state of the 3D simulation after relaxation. Solid and dashed lines represent the distribution at the loop axis ($x = 0$, $y = 0$) and the external loop region ($x = 8$Mm, $y = 0$), respectively.

To solve the 3D ideal MHD equations, we employ the PLUTO code (Mignone et al. 2007). A piecewise linear scheme is used for spatial reconstruction. Numerical fluxes are computed by the Roe Riemann solver, and a second-order characteristic tracing method is used for time marching. The hyperbolic divergence cleaning method is adopted to ensure the divergence-free nature of the magnetic field. Anisotropic thermal conduction is included in our simulations. In the 2D run, the computational domain is $[0, 6]$Mm $\times$ $[0, 100]$Mm. We consider 128 uniformly spaced cells in the r-direction and a uniform grid of 1024 cell points in the z-direction. In the 3D case, the simulation domain is $[-6, 6]$Mm $\times$ $[-3, 3]$Mm $\times$ $[0, L/2]$. We consider uniform 1024 cell points in the z-direction and 256 uniformly spaced cells in the x-direction and 128 uniform grid cells in the y-direction. The resolution in the x, y plane is about 46.9km. Although increasing the transverse resolution may reveal more pronounced heating effects, the main findings of the current work are not expected to be influenced. On one hand, the changing width of the boundary layer allows the current resolution to sufficiently resolve fine structures away from the loop apex [2]. On the other hand, the turbulent structures generated in the model will further extend the thickness of the boundary layer, making it more feasible to reveal small scales within it. The vertical resolution seems lower than that in the transverse direction. Nevertheless, it is enough to resolve the broadened transition region that is more than 2Mm wide after relaxation, considering the broadening scheme described above.

In the 2D simulation, an axisymmetric (outflow) boundary is employed at $r = 0$ ($r = 100$Mm). A symmetric boundary condition is used at $z = 100$Mm, considering the symmetric property of the fundamental kink mode considered in this study. At the bottom of the loop, the density and pressure are extrapolated from the hydrostatic equilibrium. The magnetic field is extrapolated following the zero normal gradient condition, as described by Karampelas et al. (2019). The vertical velocity v_z is set to be zero, while the transverse velocity v_r is to be outflow. In the 3D case, all the lateral boundaries are set to be outflow. Boundary conditions in the z-direction are kept the same as in the 2D except for the transverse velocity v_x and v_y at $z = 0$, which are described by a continuous

---

[2] Even at the loop apex, we can still observe relatively larger KHI structures, as shown in Figure 3b and related animations.

and monoperiodic driver (Pascoe et al. 2010; Karampelas et al. 2017; Guo et al. 2019a). In the current study, the driver period is 288s, which matches the eigenfrequency of the loop at the initial state. Note that the initial eigenfrequency of the loop slightly varies over time during the driving phase. Due to the modest changes in the density structure in the current model, the variation in eigenfrequency is not significant. Nonetheless, a broad-band driver (e.g., Afanasyev et al. 2019) needs further study and discussion. The amplitude of the driver is chosen to be 0 (non-driven model) and $4\mathrm{kms}^{-1}$ (driven model). These two models are mentioned hereafter by using subscripts "0" and "4", respectively.

3. RESULTS

We first examine the dynamic process of the loop. Figure 3 shows the isocontours of density and temperature for both models at $t = 8060\mathrm{s}$ when the loop has fully evolved. The TWIKH rolls are clearly seen from the density and temperature distribution at the apex of the driven loop in Figure 3b. The core of the loop cross-section is sufficiently heated at the loop apex, even though the Ohmic dissipation is smaller than that near the loop footpoints. To further examine the evolution in the vertical direction, surface averaged temperature and density are examined along the z-direction, which are given by

$$\bar{T}(z,t) = \frac{1}{A} \int_A T \mathrm{d}A, \bar{\rho}(z,t) = \frac{1}{A} \int_A \rho \mathrm{d}A. \tag{4}$$

where A represents the surface area of the region $-6\mathrm{Mm} \leq x \leq 6\mathrm{Mm}, -3\mathrm{Mm} \leq y \leq 3\mathrm{Mm}$ at given heights. $\mathrm{d}A$ is the surface element of the plane. Figure 4a,b show the changes in $\left(\bar{T} - \bar{T}_0\right)/\bar{T}_0$ and $\left(\bar{\rho} - \bar{\rho}_0\right)/\bar{\rho}_0$, which clearly reveal the variations caused by waves in comparison to the non-driven case. To reveal the evaporation from the lower atmosphere, the enthalpy flux and mass flux are also considered as

$$\bar{E}(z,t) = \frac{1}{A} \int_0^t \int_A \left(\frac{\gamma}{\gamma - 1} p\right) v_z \mathrm{d}A \mathrm{d}t, \tag{5}$$

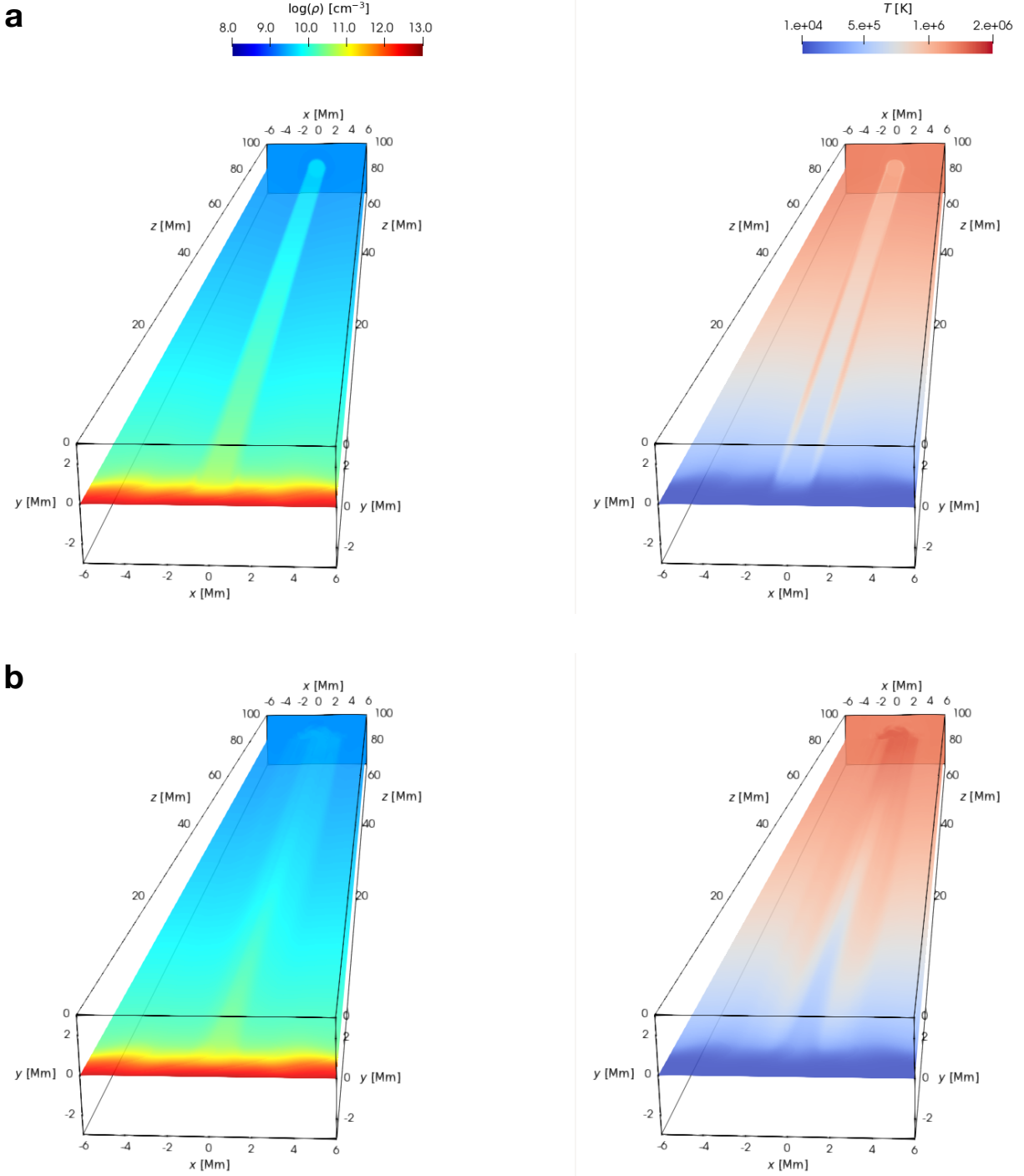$$\bar{M}(z,t) = \frac{1}{A} \int_0^t \int_A \rho v_z \mathrm{d}A \mathrm{d}t. \tag{6}$$

Figure 3. Isosurfaces of the logarithm of density and temperature at the loop apex ($z = 100$Mm) and $y = 0$ for (a) non-driven and (b) driven model at $t = 8060$s. An animation of the density and temperature isosurfaces for the driven model is available in the online Journal. The animation proceeds from $t = 0$ to 9340s.
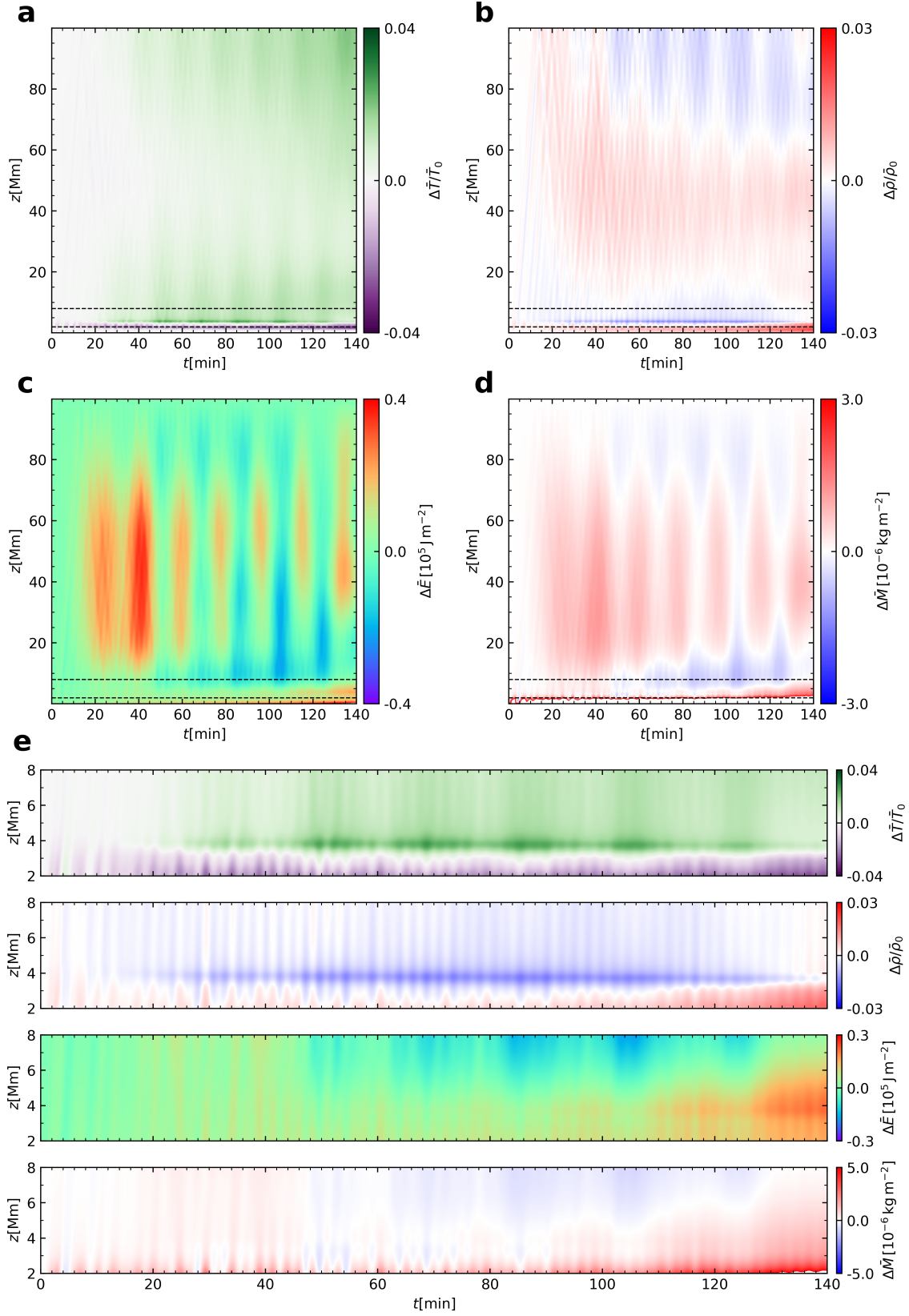
Figure 4. Surface-averaged temperature, density, enthalpy flux, and mass flux changes relative to the non-driven case are shown versus height, with zoomed-in lower panels for the regions outlined by dashed boxes.

Figure 4c shows the changes of the z-component of the enthalpy flux ($\Delta \bar{E} = \bar{E} - \bar{E}_0$). From Figure 4a, we observe the expected temperature increases near the loop footpoint. This heating induces upward enthalpy flows, as seen in Figure 4c. The upward enthalpy flows are present throughout the simulation, although periodic downward flows occur after about 50min. Figure 4b confirms the mass changes induced by the upward flow, as evidenced by the density increases. A periodicity of ~ 20min [3] of the temperature profile is observed. The density and enthalpy flux exhibit a similar periodicity as shown in Figure 4. This periodicity is associated with the ponderomotive force and is attributed to slow waves, which has also been observed in previous numerical studies (e.g., Magyar & Van Doorsselaere 2016; Karampelas et al. 2017). This has also been confirmed by Van Damme et al. (2020) by considering an Alfvén wave driver. The excited slow oscillation can influence the vertical distribution of the temperature profile, density distribution, and enthalpy flux. The variations in the temperature and density profiles relative to the non-driven case seem slight (less than 4%). This is partly because the evaporation induced by waves, as demonstrated in Van Damme et al. (2020), can only cause modest variations in the dramatically changing atmosphere background in the vertical direction. In addition, the surface averaged values here are naturally smaller than the local quantity values in the loop region, which is no longer straightforward to quantify since our current loop is fully deformed and transversely diffused than previous coronal models. Nevertheless, the surface average procedure can still reveal the average variations of quantities of loop cross-section at a given height. The evolutions of quantities in the domain of $2\text{Mm} \leq z \leq 8\text{Mm}$ are zoomed in and presented in the lower panels of Figure 4. We see upward enthalpy flows in this domain, indicating the occurrence of chromospheric evaporation. The density drops and temperature increases around $z = 4\text{Mm}$ are the consequence of this evaporation. Additionally, the lower region presents a decrease (increase) in temperature (density) variations around $z = 2\text{Mm}$. Seen from Figure 2, the boundary between the chromosphere and the transition region shifts downward to about $z = 1\text{Mm}$, while the lower boundary of the transition region outside the loop is around $z = 2\text{Mm}$. This means that denser

---

[3] This period is close to the slow transit time in the coronal counterpart.

and cooler masses from the external loop region are involved when computing the surface averaged quantities around $z = 2\text{Mm}$.

Heating effects induced by kink waves can be quantified by energy analysis (e.g., Karampelas et al. 2017; Guo et al. 2019a,b). The continuous driving at the loop footpoint changes the equilibrium compared with the non-driven case, leading to the transition region moving with time. We thus consider an upper region starting from 9Mm as the coronal counterpart in the following analysis. The volume-averaged Poynting flux and internal energy are given by

$$S(t) = -\frac{1}{V} \int_0^t \int_{A_1'} \frac{1}{\mu_0} \left[(\boldsymbol{v} \times \boldsymbol{B}) \times \boldsymbol{B} \right] \cdot \mathrm{d}\boldsymbol{A}_1' \mathrm{d}t, \tag{7}$$

$$I(t) = \frac{1}{V} \int_V \frac{p}{\gamma - 1} \mathrm{d}V - \frac{1}{V} \int_0^t \int_{A_2'} \left(\frac{\rho v^2}{2} + \rho \Phi + \frac{\gamma p}{\gamma - 1} \right) \boldsymbol{v} \cdot \mathrm{d}\boldsymbol{A}_2' \mathrm{d}t, \tag{8}$$

where V represents the volume of the concerned domain ($-6\text{Mm} \leq x \leq 6\text{Mm}, -3\text{Mm} \leq y \leq 3\text{Mm}, 9\text{Mm} \leq z \leq 100\text{Mm}$). $\mathrm{d}\boldsymbol{A}_1'$ ($\mathrm{d}\boldsymbol{A}_2'$) is the normal vector of the bottom (lateral) surface. We also incorporate the energy fluxes of lateral boundaries into the internal energy variations, following a similar procedure in Karampelas et al. (2019). The input energy is defined as the Poynting flux of the bottom interface. As aforementioned, an enthalpy flux can be seen through the bottom boundary ($z = 9\text{Mm}$) of the concerned domain. However, this enthalpy flux is much smaller than the Poynting flux here, thus has been neglected when considering the input energy from the bottom. Figure 5 shows the volume averaged energy density changes relative to the initial state, namely $S(t) - S(0)$ and $I(t) - I(0)$. In the non-driven model, the internal energy (I_0) drops with time due to the thermal conductive loss in the corona, while the internal energy variation in our driven model (I_4) stays positive before 120min and approaches zero after about 120min. This means that the internal energy first increases and then asymptotically approaches the initial equilibrium state by the end of the simulation. Therefore, the heating induced by waves can overcome or balance the thermal conductive loss in the corona, for the duration of the driving in the current model.

Heating efficiency can be evaluated by considering the ratio between the relative internal energy increase and the input energy. Figure 5 also shows the difference between the driven and non-
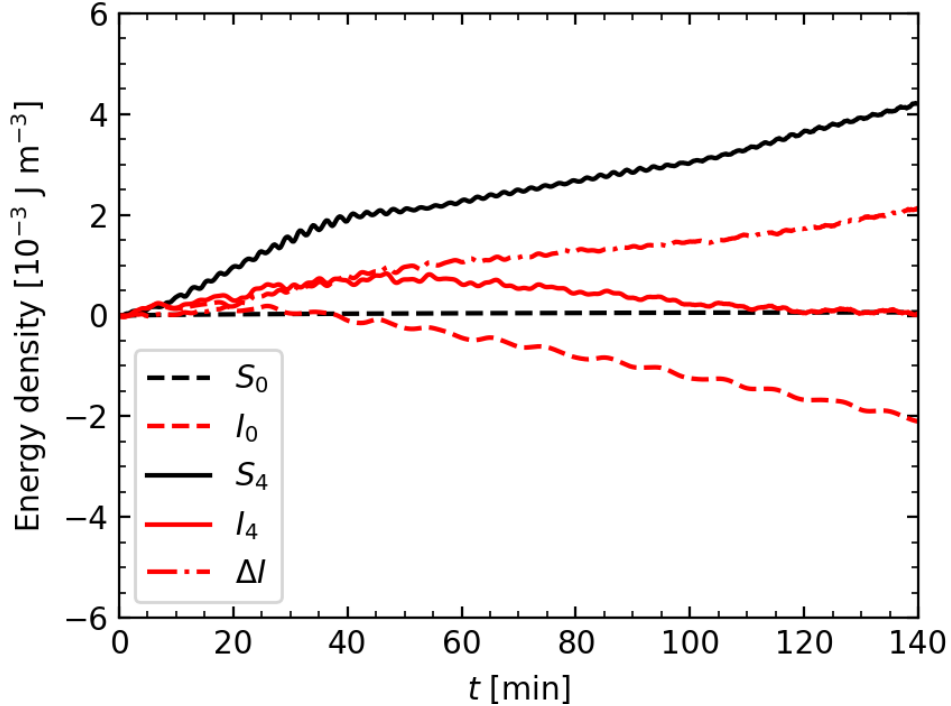
Figure 5. Volume averaged input energy (black) and internal energy density (red) changes relative to the initial state in the coronal counterpart ($-6\mathrm{Mm} \leq x \leq 6\mathrm{Mm}, -3\mathrm{Mm} \leq y \leq 3\mathrm{Mm}, 9\mathrm{Mm} \leq z \leq 100\mathrm{Mm}$). Subscript "0" ("4") denotes the non-driven (driven) model. Dot-dashed line shows the difference between the two models in the concerned domain.

driven models in the same domain. From the Poynting flux and the difference in internal energy changes, we can compute the heating efficiency of the driven model. A rapid increase in Poynting flux before 40min can be observed, leading to an average input energy flux of about $78.1\mathrm{Jm}^{-2}\mathrm{s}^{-1}$ over the considered coronal counterpart of the loop. The average internal energy increasing rate is about $32.8\mathrm{Jm}^{-2}\mathrm{s}^{-1}$, leading to a heating rate of 42%. In previous studies (e.g., Guo et al. 2019a; Karampelas et al. 2019), we report the expansion of the loop cross-section when small scales and turbulence developed, inducing a decrease in the local magnetic field. This decrease can also be traced down from the corona to lower heights with decreasing strength. The variations of the magnetic field in the lower interface between the corona and the transition region cause a slower increase of the input energy from $t \sim 50$min, leading to an average input energy flux of about $30.7\mathrm{Jm}^{-2}\mathrm{s}^{-1}$ from

$50\text{min} \leq t \leq 100\text{min}$. The corresponding internal energy growth rate is $16.8\text{Jm}^{-2}\text{s}^{-1}$ and the heating rate increases to 55%. In the last 20 minutes of the simulation, the loop is fully evolved and the expansion is saturated, we see the input energy flux increase to $45.1\text{Jm}^{-2}\text{s}^{-1}$. The corresponding internal energy increasing rate of this phase is $34.5\text{Jm}^{-2}\text{s}^{-1}$, leading to a heating rate of 76.5%. This shows a significant heating efficiency of the current model. Comparing with our previous models (e.g., Karampelas et al. 2017, 2019; Guo et al. 2019a,b; Shi et al. 2021), the presence of thermal conduction allows enthalpy flows from the lower atmosphere to the corona. Such flows change the vertical density and temperature distribution in the coronal counterpart of the loop (Figure 4). The energy dissipation at the loop cross-section becomes more efficient, as indicated by the temperature increase in Figure 3. Therefore, the upward evaporation flows lead to a more efficient heating to balance the thermal conductive losses in the current model.

4. DISCUSSION AND SUMMARY

We model a three-dimensional magnetic cylinder in a realistic solar atmosphere from the chromosphere to the corona with thermal conduction included. Frequently observed kink oscillations are excited in this magnetic flux tube. Based on previous studies, heating effects are expected due to the presence of the Kelvin-Helmholtz instability induced by kink oscillations. Temperature and internal energy increases are indeed observed in the coronal counterpart of our driven model, with respective to a non-driven case. With the inclusion of thermal conduction, chromospheric evaporation can be observed, leading to an increase in temperature and a decrease in density. Although the spatially averaged density and temperature changes are gentle ($\sim 4\%$ relative to the non-driven case), the corresponding enthalpy flow from the lower atmosphere can still influence the energy dissipation in the corona by redistributing the vertical density structuring. The efficient heating in the coronal counterpart of the loop can balance the thermal conductive loss in the current model, and thus maintain the internal energy in the corona.

In the current simulation, we adopt an approximate model derived from Aschwanden & Schrijver (2002) to describe the vertical distribution of the solar atmosphere. This temperature distribution seems a coarser approximation than the VAL model (Vernazza et al. 1981) or its upgraded versions

(Avrett & Loeser 2008). Especially, it lacks sufficient details in the lower atmosphere. Nevertheless, it describes the main properties of the parameters (e.g., temperature and density) of the chromosphere and the transition region. In addition, note that the initial analytical profiles of temperature and density change after relaxation and a new equilibrium is achieved, as shown in Figure 2b. The initial expressions of the VAL model of the atmosphere would also be changed after the relaxation.

Explicit resistivity and viscosity are not included in the current ideal MHD computation. In the solar corona, the magnetic Reynolds number is of the order of 10^{12}, leading to an extremely small resistivity if considering typical spatial scales and Alfvén speed in the corona. In practical coronal models, however, even the numerical resistivity is several orders larger than the realistic value. Given the numerical resolution limitation, we should treat such models, especially large 3D models, as an ideal approximation to the real corona. Nevertheless, to examine the influence of explicit resistivity/viscosity on wave energy dissipation is still necessary. Howson et al. (2017) found that enhanced resistivity and viscosity that are larger than numerical values can suppress the onset of TWIKH rolls, thus reducing wave energy dissipation. The influence of explicit dissipation coefficients on wave heating has been quantitatively examined by Karampelas et al. (2019). Comparing with ideal simulations with only numerical dissipation, the heating effects are enhanced but the heating locations are the same in the resistive/viscous models in Karampelas et al. (2019). This confirms that the numerical dissipation can also play an effective role in such modeling associated with waves heating effects.

In previous studies (e.g., Ofman et al. 1998), resonant absorption and phase mixing are believed to happen in resonant layers near a loop boundary. Cargill et al. (2016) believed that the resonant layer is not sustained due to the temporal evolution of the density gradient induced by Alfvén waves. In our current results, however, TWIKH rolls spread over the whole cross section of the loop, associated with chromospheric evaporation not only happening near the boundary layer, but rather in the entire loop. Nevertheless, due to the slight density and temperature changes, the evaporation has no significant effect on the resonance conditions of the current model.

In this simulation we are continuously driving waves at the eigenfrequency of the standing mode, and so the resultant evaporations may be viewed as an upper limit to the evaporations which would result from realistic, small amplitude (decayless) kink waves which are not so carefully driven. The limitation of current-day 3D MHD simulations having a magnetic Reynolds number several orders of magnitude off that for the corona further reinforces our results as an upper limit.

The realistic thermal conductive loss in the quiet solar corona is about 200J m^{-2} s^{-1} (Withbroe & Noyes 1977). The input energy in our current model does not seem to be able to complement such a high conductive loss in the real corona. However, it should be noted that the magnetic field strength of the current model is still vertically uniform. In reality, if the loop footpoint is anchored in the photosphere, the magnetic field should be much (or even several orders of magnitude) larger than that in the corona. This probably indicates that the real energy input from the photosphere is sufficient. In fact, observations have confirmed that the energy flux is indeed sufficient to balance the energy losses even in the active region (e.g., Fujimura & Tsuneta 2009).

We have simulated a more realistic coronal loop by including a dense and cold chromosphere, and despite the additional dynamics and energetics, it is encouraging to see that the results about wave heating inferred from coronal-only simulations still seems to hold. Examples include the formation of extended TWIKH rolls along the whole loop; and the increased efficiency of wave heating once the kinetic energy saturates at the later stages of the simulation and a turbulent density profile has developed.

REFERENCES

Afanasyev, A., Karampelas, K., & Van
    Doorsselaere, T. 2019, ApJ, 876, 100.
    doi:10.3847/1538-4357/ab1848

Antolin, P., Okamoto, T. J., De Pontieu, B., et al.
    2015, ApJ, 809, 72.
    doi:10.1088/0004-637X/809/1/72

Arregui, I. 2015, Philosophical Transactions of the
    Royal Society of London Series A, 373, 20140261.
    doi:10.1098/rsta.2014.026110.48550/arXiv.1501.06708

Aschwanden, M. J. & Schrijver, C. J. 2002, ApJS,
    142, 269. doi:10.1086/341945

Avrett, E. H. & Loeser, R. 2008, ApJS, 175, 229.
    doi:10.1086/523671

Bradshaw, S. J. & Cargill, P. J. 2010, ApJL, 710,
    L39. doi:10.1088/2041-8205/710/1/L39

Browning, P. K. & Priest, E. R. 1984, A&A, 131,
    283

Cargill, P. J., Bradshaw, S. J., & Klimchuk, J. A.
    2012, ApJ, 752, 161.
    doi:10.1088/0004-637X/752/2/161

Cargill, P. J., De Moortel, I., & Kiddie, G. 2016,
    ApJ, 823, 31. doi:10.3847/0004-637X/823/1/31

De Moortel, I. & Nakariakov, V. M. 2012,
    Philosophical Transactions of the Royal Society
    of London Series A, 370, 3193.
    doi:10.1098/rsta.2011.064010.48550/arXiv.1202.1944

De Moortel, I. & Howson, T. A. 2022, ApJ, 941,
    85.doi:10.3847/1538-4357/aca072

Fisher, G. H., Canfield, R. C., & McClymont,
    A. N. 1985, ApJ, 289, 414. doi:10.1086/162901

Fisher, G. H., Canfield, R. C., & McClymont,
    A. N. 1985, ApJ, 289, 425. doi:10.1086/162902

Fujimura, D. & Tsuneta, S. 2009, ApJ, 702, 1443.
    doi:10.1088/0004-637X/702/2/1443

Goossens, M., Erdélyi, R., & Ruderman, M. S.
    2011, SSRv, 158, 289.
    doi:10.1007/s11214-010-9702-7

Guo, M., Van Doorsselaere, T., Karampelas, K.,
    et al. 2019, ApJ, 870, 55.
    doi:10.3847/1538-4357/aaf1d0

Guo, M., Van Doorsselaere, T., Karampelas, K.,
    et al. 2019, ApJ, 883, 20.
    doi:10.3847/1538-4357/ab338e

Guo, M., Li, B., & Van Doorsselaere, T. 2020,
    ApJ, 904, 116. doi:10.3847/1538-4357/abc1df

Heyvaerts, J. & Priest, E. R. 1983, A&A, 117, 220

Howson, T. A., De Moortel, I., & Antolin, P.
    2017, A&A, 602, A74.
    doi:10.1051/0004-6361/201630259

Karampelas, K., Van Doorsselaere, T., & Antolin,
    P. 2017, A&A, 604, A130.
    doi:10.1051/0004-6361/201730598

Karampelas, K. & Van Doorsselaere, T. 2018,
    A&A, 610, L9.
    doi:10.1051/0004-6361/201731646

Karampelas, K., Van Doorsselaere, T., & Guo, M.
    2019, A&A, 623, A53.
    doi:10.1051/0004-6361/201834309

Karampelas, K., Van Doorsselaere, T., Pascoe, D. J., et al. 2019, Frontiers in Astronomy and Space Sciences, 6, 38. doi:10.3389/fspas.2019.00038

Linker, J. A., Lionello, R., Mikić, Z., et al. 2001, J. Geophys. Res., 106, 25165. doi:10.1029/2000JA004020

Lionello, R., Linker, J. A., & Mikić, Z. 2009, ApJ, 690, 902. doi:10.1088/0004-637X/690/1/902

Magyar, N. & Van Doorsselaere, T. 2016, A&A, 595, A81.doi:10.1051/0004-6361/20162901010.48550/arXiv.1609.06883

Mikić, Z., Lionello, R., Mok, Y., et al. 2013, ApJ, 773, 94. doi:10.1088/0004-637X/773/2/94

Milligan, R. O., Gallagher, P. T., Mathioudakis, M., et al. 2006, ApJL, 638, L117. doi:10.1086/50055510.48550/arXiv.astro-ph/0509664

Mignone, A., Bodo, G., Massaglia, S., et al. 2007, ApJS, 170, 228. doi:10.1086/513316

Nakariakov, V. M. & Kolotkov, D. Y. 2020, ARA&A, 58, 441. doi:10.1146/annurev-astro-032320-042940

Nakariakov, V. M., Anfinogentov, S. A., Antolin, P., et al. 2021, SSRv, 217, 73. doi:10.1007/s11214-021-00847-2

Ofman, L., Davila, J. M., & Steinolfson, R. S. 1994, Geophys. Res. Lett., 21, 2259. doi:10.1029/94GL01416

Ofman, L., Klimchuk, J. A., & Davila, J. M. 1998, ApJ, 493, 474. doi:10.1086/305109

Parker, E. N. 1988, ApJ, 330, 474. doi:10.1086/166485

Pascoe, D. J., Wright, A. N., & De Moortel, I. 2010, ApJ, 711, 990. doi:10.1088/0004-637X/711/2/990

Pelouze, G., Van Doorsselaere, T., Karampelas, K., et al. 2023, arXiv:2301.03100

Shi, M., Van Doorsselaere, T., Guo, M., et al. 2021, ApJ, 908, 233. doi:10.3847/1538-4357/abda54

Soler, R. & Terradas, J. 2015, ApJ, 803, 43. doi:10.1088/0004-637X/803/1/43

Terradas, J., Andries, J., Goossens, M., et al. 2008, ApJL, 687, L115. doi:10.1086/593203

Tian, H. & Chen, N.-H. 2018, ApJ, 856, 34. doi:10.3847/1538-4357/aab15a

Van Damme, H. J., De Moortel, I., Pagano, P., et al. 2020, A&A, 635, A174. doi:10.1051/0004-6361/201937266

Van Doorsselaere, T., Andries, J., & Poedts, S. 2007, A&A, 471, 311. doi:10.1051/0004-6361:20066658

Van Doorsselaere, T., Srivastava, A. K., Antolin, P., et al. 2020, SSRv, 216, 140. doi:10.1007/s11214-020-00770-y

Van Doorsselaere, T., Goossens, M., Magyar, N., et al. 2021, ApJ, 910, 58. doi:10.3847/1538-4357/abe630

Vernazza, J. E., Avrett, E. H., & Loeser, R. 1981, ApJS, 45, 635. doi:10.1086/190731

Withbroe, G. L. & Noyes, R. W. 1977, ARA&A,

   15, 363.

   doi:10.1146/annurev.aa.15.090177.002051